Supplemental Information:

Charge Distribution Uncertainty in Differential Mobility Analysis of Aerosols

Johannes Leppä, Wilton Mui, Amanda M. Grantz and Richard C. Flagan

Appendix

A1 Ion mobility distributions

The mobility distribution of the ions produced in a TSI 3077 bipolar ^{85}Kr aerosol charger was measured in laboratory conditions at Caltech in Pasadena, CA (T = 298.15 K, p = 96757 Pa). HEPA-filtered, particle-free, room air was directed into the charger and the ions exiting the charger were segregated according to their electrical mobility using a Radial Opposed Migration Ion and Aerosol Classifier, ROMIAC (Mui et al. 2013; Mui et al. 2017), with a TSI 3068 electrometer used for detecting the ions. The measurement covered the mobility range from 0.1 $cm^2V^{-1}s^{-1}$ to 5.9 $cm^2V^{-1}s^{-1}$. All the plumbing of the instrumentation setup was stainless steel. The sample flow rate was 2.25 lpm and the cross-flow rate was 20 lpm, for a non-dispersive resolution of 8.9.

The data was inverted using a transfer function derived for a rectilinear opposed migration aerosol classifier (OMAC; Flagan 2004) following the flux coordinate method of Stolzenburg (1988) for deriving the transfer function for a cylindrical differential mobility analyzer. The derivation of the OMAC transfer function was described in detail by Mai (2016) and is applied by Mui et al. (2017) in a comprehensive characterization of the instrument using high mobility electrosprayed tetralkyl ammonium halide ions as small as 1.16 nm in mobility diameter. The ROMIAC transfer function, with explicit correction factors for the ROMIAC, is

$$\Omega = \frac{\sqrt{\tilde{\sigma}^2+\tilde{\sigma}^2_{\mathrm{distor}}}}{\sqrt{2}B\gamma_B(1-\delta)}\left[\mathcal{E}\left(\frac{\tilde{Z}-(1+B\gamma_B)}{\sqrt{2}\sqrt{\tilde{\sigma}^2+\tilde{\sigma}^2_{\mathrm{distor}}}}\right)+\mathcal{E}\left(\frac{\tilde{Z}-(1-B\gamma_B)}{\sqrt{2}\sqrt{\tilde{\sigma}^2+\tilde{\sigma}^2_{\mathrm{distor}}}}\right)-\mathcal{E}\left(\frac{\tilde{Z}-(1+\delta B\gamma_B)}{\sqrt{2}\sqrt{\tilde{\sigma}^2+\tilde{\sigma}^2_{\mathrm{distor}}}}\right)-\mathcal{E}\left(\frac{\tilde{Z}-(1-\delta B\gamma_B)}{\sqrt{2}\sqrt{\tilde{\sigma}^2+\tilde{\sigma}^2_{\mathrm{distor}}}}\right)\right] \quad [S1]$$

where $\tilde{\sigma}$ is a dimensionless measure of diffusional broadening, evaluated as an integral (which is a function of the operating flow rates, voltage, and classifier geometry) along the ion migration path, B is the ratio of the sample flow rate to the cross-flow rate, δ is the flow rate ratio imbalance, $\tilde{Z} = Z/Z^*$ is the

dimensionless mobility, where Z is the mobility and Z^* is the nominal ion mobility transmitted by the ROMIAC at a given cross-flow rate and voltage setting, $\tilde{\sigma}^2_{\text{distor}}$ and γ_B are correction factors for $\tilde{\sigma}$ and B, respectively, for the ROMIAC due in part to its radial geometry, and

$$\mathcal{E}(y) = y\,\text{erf}(y) + \pi^{-1/2}\exp(-y^2). \qquad \text{[S2]}$$

The electrosprayed ions were also used to characterize the ROMIAC efficiency, which has been found to empirically follow a function of the ion mobility and flow rate ratio. Mui et al. (2017) also measured the transmission efficiency of high mobility ions in the ROMIAC; for the flow rate ratio in this work, the transmission efficiency of 1–2 nm ions ranges from 6–23 %.

The inversion algorithm used for obtaining the ion mobility distribution is the same as that used for inferring particle size distributions from the synthetic signals in Section 2.4 in the main text, with the difference being that the ROMIAC transfer function and measured transmission efficiencies were incorporated into the inversion algorithm, as opposed to using the pseudo-instrument transfer function.

In the measured mobility distribution of the negative charger ions, $n_i^-(Z_i)$, we observed one major peak, at the mobility of ~1.5 $cm^2V^{-1}s^{-1}$, which contributed over 99 % of the negative ions (Figure S1). The observed mean and median mobilities were $Z_{i,ave}^-$ = 1.53 and $Z_{i,med}^-$ = 1.56 $cm^2V^{-1}s^{-1}$, respectively. The mobility distribution of positive ions, $n_i^+(Z_i)$, however, was considerably more continuous, with the major peak, at mobility of ~1.2 $cm^2V^{-1}s^{-1}$, contributing ~84 % of the negative ions. The observed mean and median mobilities were $Z_{i,ave}^+$ = 1.12 and $Z_{i,med}^+$ = 1.12 $cm^2V^{-1}s^{-1}$, respectively. The signal from particles with d_p > 1.9 nm would not be affected due to charger ions being detected in addition to the particles, but a slightly more conservative lower limit of 2 nm was used for the particle size distribution in this study.

Filtered ambient lab air was transported through stainless steel tubing in this study, but another choice of sampled gas mixture or plumbing material used would have likely resulted in a different $n_i^\pm(Z_i)$ (Steiner and Reischl 2012; Steiner et al. 2014; Maißer et al. 2015). In order to probe the effect of ion mobility distribution on the charge distribution, and, consequently, on the biases in the particle size distribution measurements due to inaccurate assumptions of the charge distribution acquired in the charger, we conducted the simulations using two different ion mobility distributions: the one according to our measurements and another based on the measurements by Steiner and Reischl (2012), which are referred to as measured and SR distributions, respectively (Figure S1).

Steiner and Reischl used different relation between ion mobility and size; the SR distribution was based on the values of electrometer current as a function of electrical mobility as reported by Steiner and Reischl (2012), but the conversion of those mobility values to diameter and mass was according to Eq. (1). For the SR distribution, the mean and median mobility of negative (positive) ions were $Z_{i,ave}^-$ = 2.14 and $Z_{i,med}^-$ = 2.19 $cm^2V^{-1}s^{-1}$ ($Z_{i,ave}^+$ = 1.66 and $Z_{i,med}^+$ = 1.66 $cm^2V^{-1}s^{-1}$,), respectively. These mean mobilities differ slightly from the corresponding values reported by Steiner and Reischl, which

were 2.09 and 1.65 $cm^2V^{-1}s^{-1}$ for negative and positive ions, respectively. This minor difference has no effect on the conclusions of this study, as the purpose of using both the measured and SR distributions is to cover the extremes of very low (measured) and high (SR) charger ion mobilities using realistic ion mobility distributions.

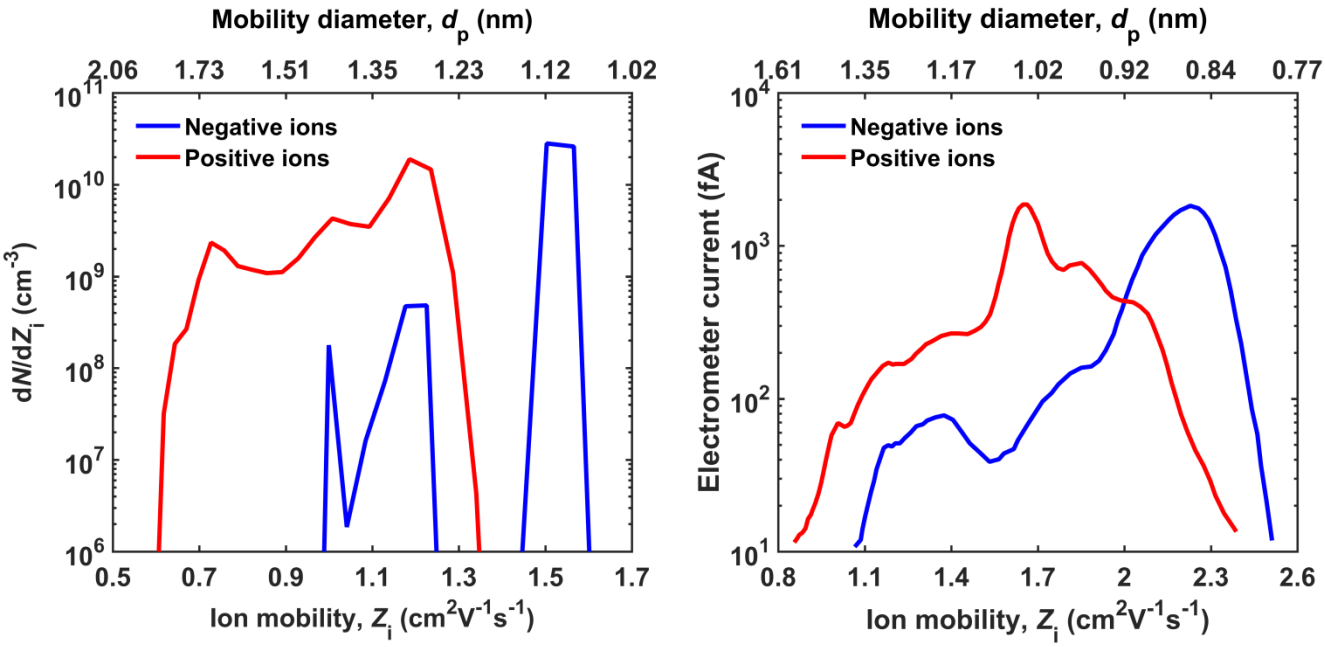

Figure S1. Left panel: The measured mobility distribution of the ions produced by ^{85}Kr aerosol charger using particle free laboratory air as the sample. Right panel: The mobility distribution of the ions produced by ^{241}Am aerosol charger using clean and dry laboratory air as the sample (Steiner and Reischl 2012). It should be noted that, unlike the mobility values, the diameter values do not match those reported by Steiner and Reischl due to different relation between mobility and size used in this study.

A2 Flux coefficients and charge distributions

A2.1 Calculation of charge distributions using effective flux coefficients

The steady-state bipolar charge distribution of an aerosol can be deduced from the ion-to-particle flux coefficients by solving a system of population balance equations (Hussin et al. 1983). A detailed derivation of the model employed in this study is given in López-Yglesias and Flagan (2013a), except that we account for the polarization of air in the ion mass-mobility relation and that, instead of considering only one type of negative and positive ion, we follow the approach taken by Lee et al. (2005) to describe the ions using a discrete mobility distribution, $n_i^{\pm}(Z_i)$. For discrete distribution

$$n_{i,T}^{\pm} = \sum_{m=1}^{x} n_{i,m}^{\pm}(Z_{i,m}), \quad [S3]$$

where $n_{i,T}$ is the total concentration of ions, $n_{i,m}^{\pm}(Z_{i,m})$ is the concentration of ions with electrical mobility $Z_{i,m}$, x is the number of mobility bins in the distribution and "+" and "-" refer to positive and negative polarity, respectively. In this case, the balance equation describing the variation of concentration of particles having charge state k, n_k, becomes

$$\frac{dn_k(d_p)}{dt} = \sum_{m=1}^{x} \beta_{k-1}^{+}(d_p, Z_{i,m}) n_{i,m}^{+}(Z_{i,m})\, n_{k-1}(d_p) - \sum_{m=1}^{x} \beta_{k}^{+}(d_p, Z_{i,m}) n_{i,m}^{+}(Z_{i,m})\, n_k(d_p) + \sum_{m=1}^{x} \beta_{k+1}^{-}(d_p, Z_{i,m}) n_{i,m}^{-}(Z_{i,m})\, n_{k+1}(d_p) - \sum_{m=1}^{x} \beta_{k}^{-}(d_p, Z_{i,m}) n_{i,m}^{-}(Z_{i,m})\, n_k(d_p) \quad [S4]$$

where t is time and $\beta_k^{\pm}(d_p, Z_i)$ is the flux coefficient of ions with mobility Z_i to particles with diameter d_p. We can now define an effective flux coefficient of the total ion mobility distribution, $\beta_{eff,k}^{\pm}(d_p)$, as

$$\beta_{eff,k}^{\pm}(d_p) = \frac{\sum_{m=1}^{x} \beta_k^{\pm}(d_p, Z_{i,m}) n_{i,m}^{\pm}(Z_{i,m})}{\sum_{m=1}^{x} n_{i,m}^{\pm}(Z_{i,m})} = \frac{\sum_{m=1}^{x} \beta_k^{\pm}(d_p, Z_{i,m}) n_{i,m}^{\pm}(Z_{i,m})}{n_{i,T}^{\pm}}. \quad [S5]$$

By using the effective flux coefficient, the balance equation simplifies to

$$\frac{dn_k(d_p)}{dt} = \beta_{eff,k-1}^{+}(d_p) n_{i,T}^{+} n_{k-1}(d_p) - \beta_{eff,k}^{+}(d_p) n_{i,T}^{+} n_k(d_p) + \beta_{eff,k+1}^{-}(d_p) n_{i,T}^{-} n_{k+1}(d_p) - \beta_{eff,k}^{-}(d_p) n_{i,T}^{-} n_k(d_p). \quad [S6]$$

In other words, with the definition of the effective flux coefficients, Eq. (S5), the balance equation accounting for the whole ion mobility distribution, Eq. (S4), reduces to a balance equation with only one variable representing all ions in the distribution, Eq. (S6). By specifying the maximum number of charges that a particle can acquire, k_{max}, the Eq. (S6) can be written for each charge state considered, and the fraction of particles with a diameter, d_p, that have the charge state k, $f_k(d_p)$, can be solved for each k from that set of balance equations (e.g., k_{max} = 5 for Hoppel and Frick (1986), and k_{max} = 100 for López-Yglesias and Flagan (2013a), and k_{max} = 30 in this study). The definition of the effective flux coefficient allows for a simplified visualization of the flux coefficients of the ion mobility distribution, as the coefficients for each ion type need not to be depicted separately, though, on the other hand, the effective flux coefficients do not correspond to any specific ion type.

A2.2 Variation in flux coefficients due to ion mobility distribution

Figure S2 shows the effective flux coefficients calculated according to Eq. (S5). For the simplicity of presentation, only the flux coefficients to particles with up to three charges are shown. While the flux coefficients are qualitatively similar for the measured and SR distributions, there are considerable differences in the values throughout the diameter range considered. Except for the fluxes to particles with d_p < 10 nm and charge state opposite to that of the ion, the flux coefficients for the SR distribution were higher than those of the measured distribution (Figure S3).

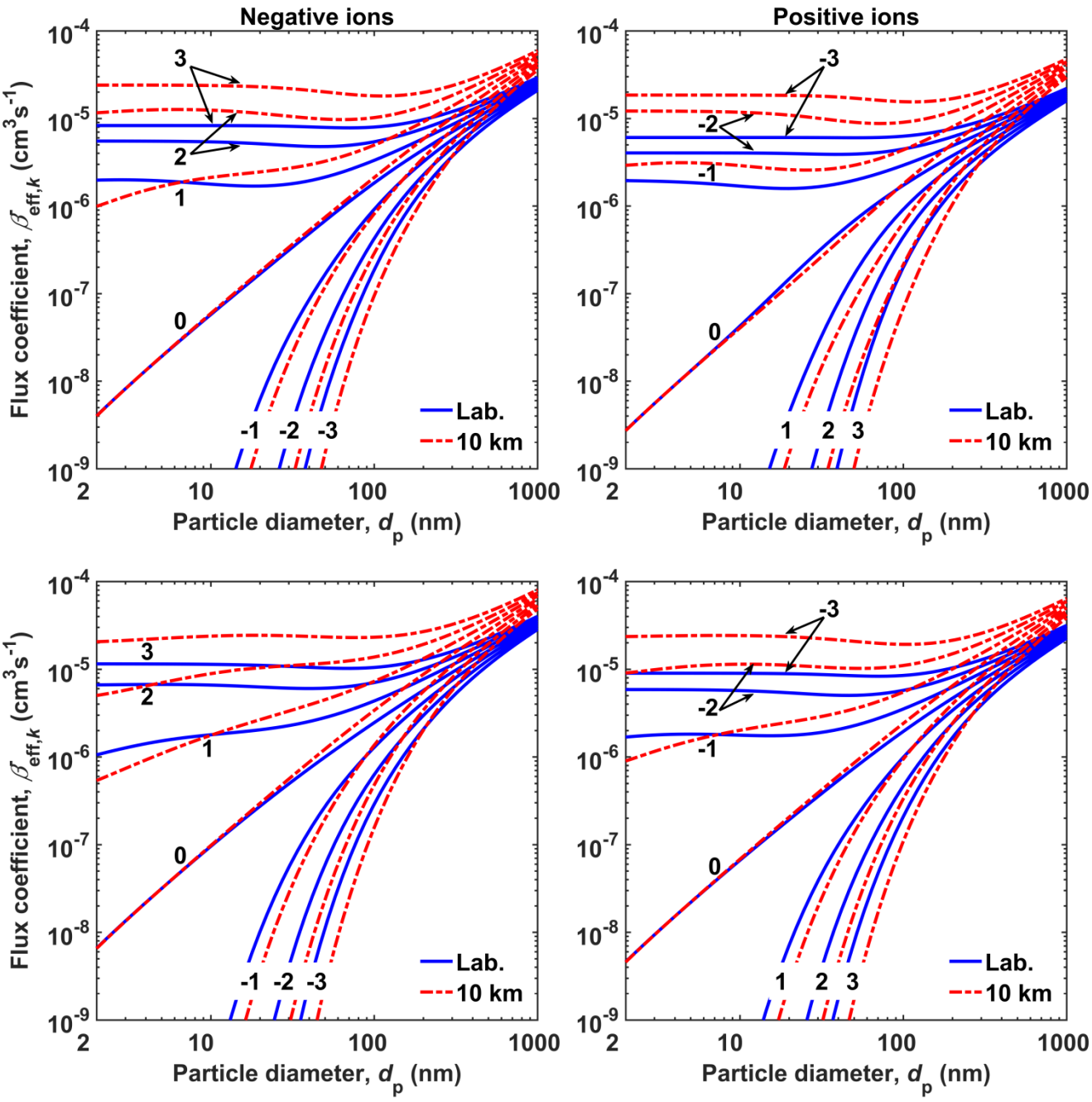

Figure S2. The effective flux coefficients, $\beta_{\mathrm{eff},k}^{\pm}$, of negative (left panels) and positive (right panels) ions to particles with k charges in T and p corresponding to the measured ion distribution (upper panels) and to the SR distribution (lower panels) at conditions at laboratory (T = 298.15 K; p = 96757 Pa; "Lab.") and at 10 km altitude (T = 223 K; p = 26500 Pa; "10 km").

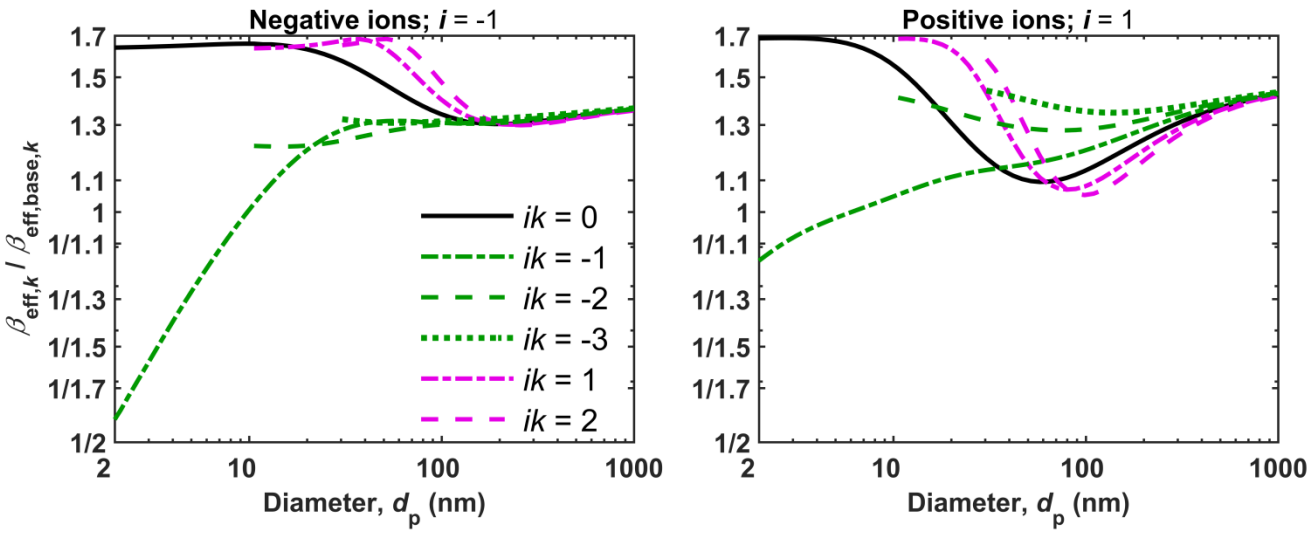

Figure S3. The ratio of effective flux coefficients of the SR distribution, β_{eff}, to those of the measured distribution, $\beta_{eff,base}$. The particle and ion charge states are denoted by k and i, respectively, with the fluxes of negative (positive) ions shown on the left (right). The particle charge states relative to the ion polarity are denoted with line style and color as indicated in the legend. The ion fluxes to particles with one similar or two opposite charges, and with two similar or three opposite charges are depicted only for particles with $d_p > 10$ nm and $d_p > 30$ nm, since doubly- and triply-charged particles, respectively, are extremely rare below these thresholds.

Particles with $d_p < 10$ nm carry at most a single charge, so their charge distribution depends only on the flux coefficients of ions to particles that are either neutral or carry a charge opposite to that of the ion. As the ion fluxes to neutral and oppositely-charged particles were higher and lower, respectively, for the SR distribution than for the measured distribution, i.e., there was more charging of neutral particles and less neutralization of charged particles, the fraction of singly-charged particles with $d_p < 10$ nm was higher for the SR distribution than for the measured distribution (Figure S4). If the charge distribution according the measured distribution was acquired in the charger, but the higher charged fraction corresponding to the SR distribution was assumed in the inversion, the concentrations of particles < 10 nm in diameter were underestimated (Figure 4).

The probability of a particle carrying multiple charges increases with increasing particle size (Figure S4). At particle sizes with considerable fractions of multiply-charged particles, it becomes complicated to interpret how the changes in the flux coefficients affect the charge distribution, since the number of equations in the form of Eq. (S6) in the system of balance equations increases with increasing k_{max}. For particles larger than 10 nm in diameter the flux coefficients were higher for the ions characterized by the SR distribution than the corresponding flux coefficients of the measured ions for vast majority of particle sizes and charge states (Figure S3). Those differences in the flux coefficients resulted in differences in the charge distribution (Figure S4). Consequently, if the charge

distribution based on the measured ions was acquired in the charger, but the one according to SR distribution was assumed in the inversion, the concentrations of particles with 10 nm < d_p < 100 nm were underestimated if negative particles were counted, while both over- and underestimation was observed for particles with d_p > 10 nm, if positive particles were counted.

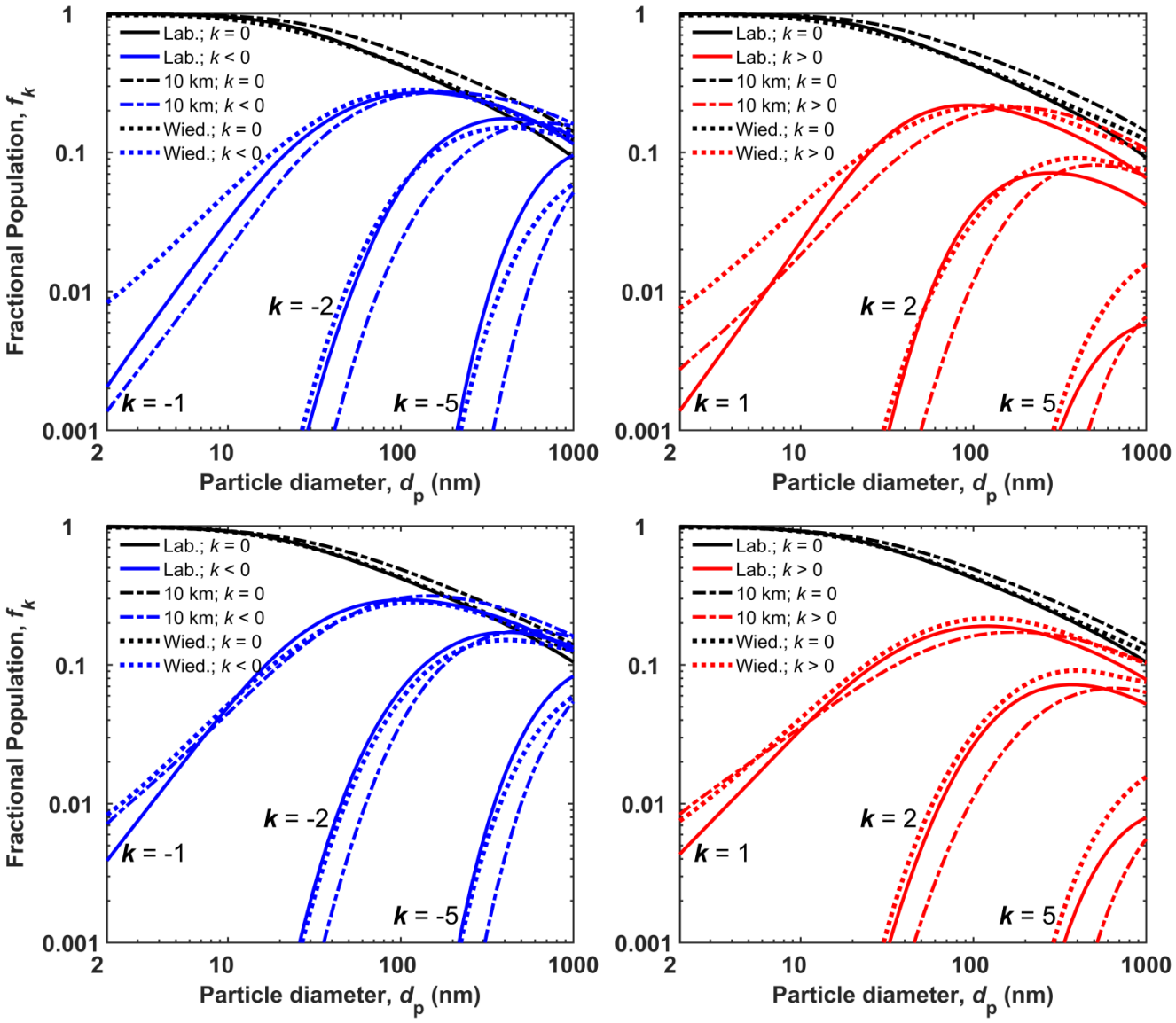

Figure S4. The charge distributions in T and p corresponding to conditions at laboratory (T = 298.15 K; p = 96757 Pa; "Lab.") and at 10 km altitude (T = 223 K; p = 26500 Pa; "10 km"), and the charge distribution according to Wiedensohler (1988; "Wied."), as indicated by line style. Fractional populations of negative (positive) particles are shown on the left (right) with k denoting the particle charge state. Data is shown for the measured (upper panels) and SR (lower panels) distributions.

A2.3 Variation in flux coefficients due to temperature and pressure

As expected based on the results by López-Yglesias and Flagan (2013b), the flux coefficients at the T and p corresponding to 10 km altitude differ significantly from those at laboratory conditions (Figure S2). Moreover, since the chemical composition of the air going into the charger affects the mobility distribution of the ions (Steiner et al. 2014; Maißer et al. 2015), the actual mobility distribution of the ions at 10 km altitude would likely differ from those in the laboratory. Assessing this difference requires data that are beyond the scope of this study.

In general, at 10 km altitude, when the measured distribution was used, the flux coefficient of ions to oppositely- and similarly-charged particles were higher and lower, respectively, than at the laboratory, and the flux coefficients at different conditions approached a different asymptote with increasing particle size (Figure S2). The variation of the flux coefficients with altitude conditions altered the charge distributions calculated for these conditions (Figure S4). Furthermore, charge distributions calculated for both conditions differed from those predicted using the parameterization by Wiedensohler (1988), which was based on the Hoppel and Frick (1986) calculations at standard temperature and pressure.

For particles with $d_p < 10$ nm the ion fluxes to neutral particles were approximately the same both in the laboratory conditions and at 10 km altitude, so the observed difference in the charge distributions in those conditions were due to variation in the ion flux to oppositely-charged particles (Figure S5). As the flux of positive ions to negative particles was consistently higher at 10 km than at laboratory, the negative particles were more rapidly neutralized resulting to lower steady-state fraction (Figure S4). Failure to take that lower fraction of negatively-charged particles into account in the inversion resulted in underestimation of concentrations of particles with $d_p < 10$ nm (Figure 5). The flux of negative ions to positive particles, however, was either smaller or larger at 10 km altitude than at laboratory, depending on particle size, which resulted in particle concentrations being either over- or underestimated, respectively.

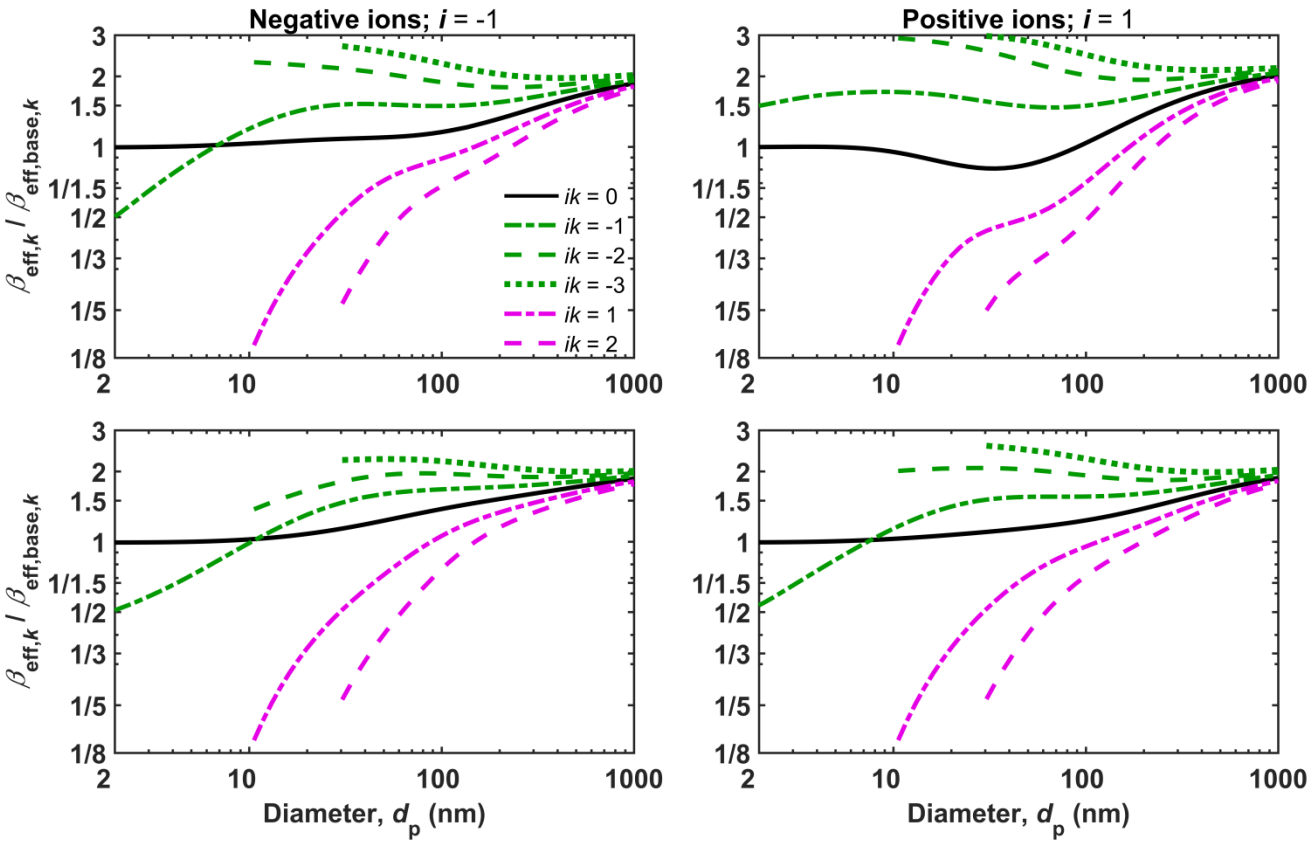

Figure S5. The ratio of effective flux coefficients at 10 km altitude, β_{eff}, to those at laboratory, $\beta_{eff,base}$. The particle and ion charge states are denoted by k and i, respectively, with the fluxes of negative (positive) ions shown on the left (right). The particle charge states relative to the ion polarity are denoted with line style and color as indicated in the legend. Data in upper and lower panels correspond to the measured and SR distributions, respectively. The ion fluxes to particles with one similar or two opposite charges, and with two similar or three opposite charges are depicted only for particles with $d_p > 10$ nm and $d_p > 30$ nm, since doubly- and triply-charged particles, respectively, are extremely rare below these thresholds.

A2.4 Variation in flux coefficients due to ion mass

Regardless of whether the measured or SR distribution was used, when the mass of ions was considerably decreased, the largest changes in the effective flux coefficients were the increases in the ion fluxes to neutral particles and to particles with charge similar to the ions, especially for particles with $d_p < 20$ nm (Figure S6). As those fluxes increase the net charge of the aerosol population, the decrease in the ion masses resulted in higher fractions of singly-charged particles with $d_p < 20$ nm, which, if not taken into account in the inversion, resulted in overestimation of the particle concentrations (Figure 6). When the measured distribution was used, this overestimation switched to underestimation at $d_p = 21$ nm, if positive particles were counted. The reason for this switch was that, at that size, the increase in the flux of positive ions to neutral particles was overtaken by the increase in

the flux of negative ions to positive particles, which resulted in decrease in the fraction of singly-charged positive particles. The same phenomenon was observed also when the SR distribution was used, though the switch occurred at d_p = 60 nm, and the magnitude of the underestimation of concentrations of particles with d_p > 60 nm was less pronounced than in the case of the measured distribution. The effects of more massive ions on the flux coefficients were opposite to the effects of less massive ions (Figure S7).

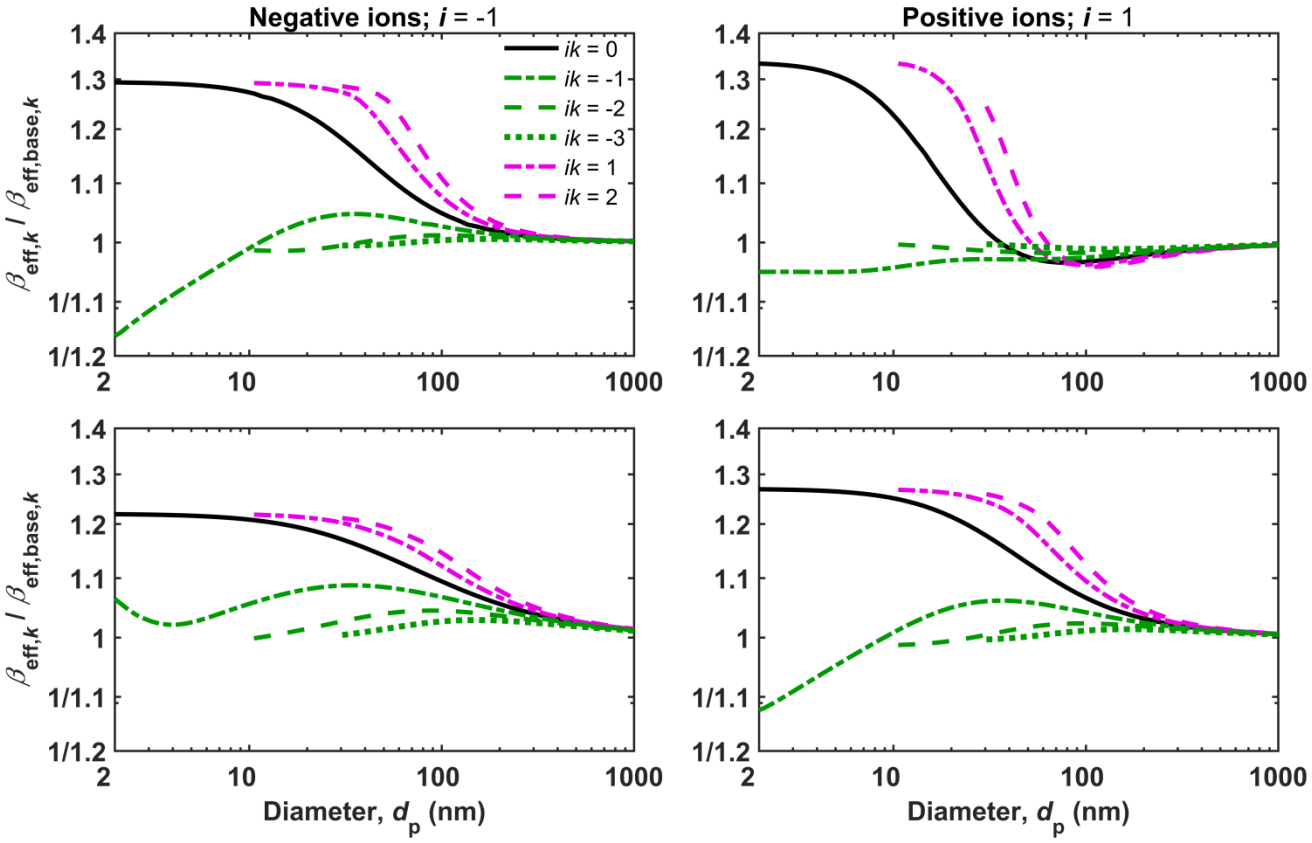

Figure S6. The same as Figure S5, except that β_{eff} and $\beta_{eff,base}$ are the effective flux coefficients of ions with masses in the range from 130 to 1000 Da and from 220 to 1800 Da, respectively, for the measured distribution (upper panels). For SR distribution (lower panels), β_{eff} and $\beta_{eff,base}$ are the effective flux coefficients of ions with masses in the range from 43 to 460 Da and from 55 to 840 Da, respectively.

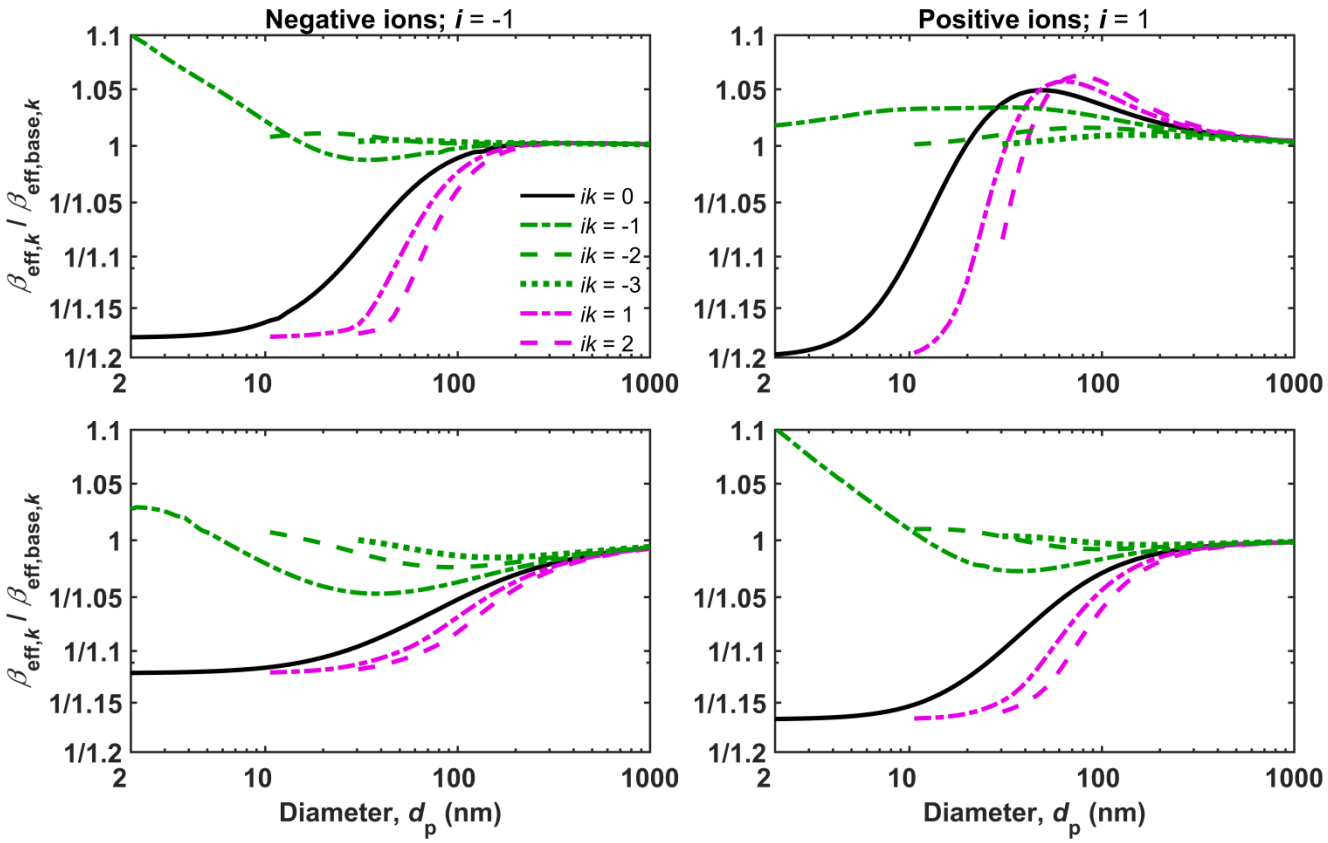

Figure S7. The same as Figure S5, except that β_{eff} and $\beta_{\mathrm{eff,base}}$ are the effective flux coefficients of ions with masses in the range from 300 to 2700 Da and from 220 to 1800 Da, respectively, for the measured distribution (upper panels). For SR distribution (lower panels), β_{eff} and $\beta_{\mathrm{eff,base}}$ are the effective flux coefficients of ions with masses in the range from 62 to 1200 Da and from 55 to 840 Da, respectively.

A2.5 Variation in flux coefficients due to relative permittivity of the particle

If the particles were made of material with low relative permittivity, such as polystyrene with $\chi_{\mathrm{p}} = 2.6$, the ion-to-particle fluxes were smaller than corresponding fluxes to conductive particles (Figure S8). The flux coefficients were smaller regardless of the particle charge state, as the decrease in the relative permittivity of the particle decreased the potential related to image charges induced on the particle, which is always an attractive potential for the system of a point charge outside of a sphere. The fluxes of ions to oppositely-charged particles, for which the Coulombic force between the net charges of the ion and the particle was attractive, were less affected than the fluxes of ions to similarly-charged particles, for which the Coulombic force between the net charges is repulsive. As a result, for particles with $d_{\mathrm{p}} < 30$ nm, the fractions of charged polystyrene particles were lower than the corresponding fractions of charged conductive particles, which, if not accounted for in the inversion, resulted in underestimation of the particle concentrations (Figure 7).

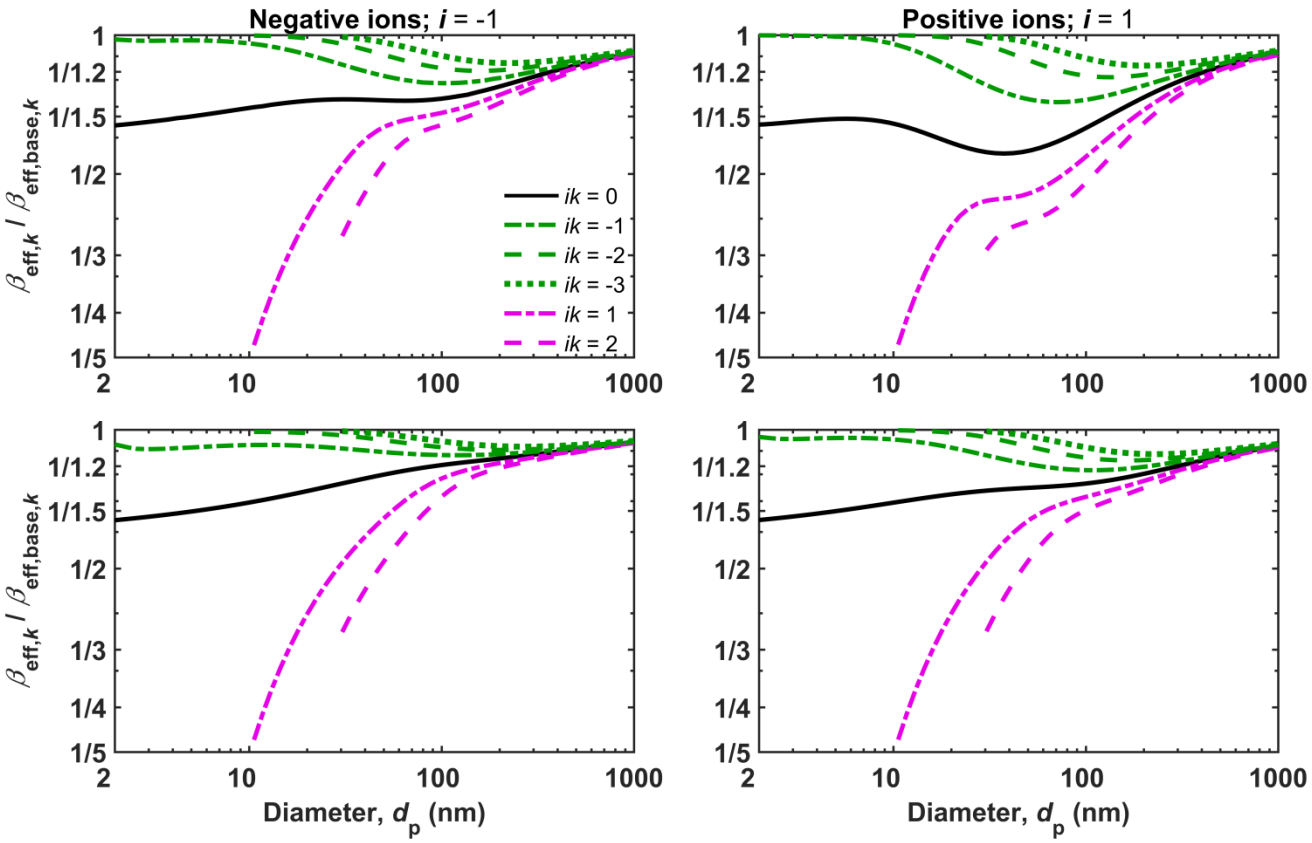

Figure S8. The same as Figure S5, except that β_{eff} and $\beta_{eff,base}$ are the effective flux coefficients of ions to polystyrene (χ_p = 2.6) and conductive ($\chi_p = \infty$) particles, respectively. The data for NaCl particles (χ_p = 6) were qualitatively the same as the data shown here for polystyrene particles, except that the ratios of β_{eff} and $\beta_{eff,base}$ were closer to unity.

A3 Additional sources of uncertainty in the inferred particle size distribution

A3.1 Bias in the inferred particle size distribution due to using mean or median mobility instead of the whole ion mobility distribution

While studies using the Brownian dynamics method to estimate the charge distribution have accounted for multiple ion species (Gopalakrishnan et al. 2013; Maißer et al. 2015; Gopalakrishnan et al. 2015), in most previous studies (e.g., Hoppel and Frick 1986; López-Yglesias and Flagan 2013b) estimating the charge distribution from the ion-to-particle flux coefficients, the ions have been modeled using a single characteristic positive and negative ion. We conducted simulations to examine the effect of this simplification. When calculating $\boldsymbol{f}_{cha}$ using the whole measured ion mobility distribution, but $\boldsymbol{f}_{inv}$ using only the mean, $Z_{i,ave}$, or median, $Z_{i,med}$, value of the mobility, little bias was observed in the particle size distribution (Figure S9). Using $Z_{i,ave}$ caused less bias than using $Z_{i,med}$: the value of $R^*_{ave}(d_p)$ was within a factor of 1.05 from unity when $Z_{i,ave}$ was used, and mostly within a factor of 1.1 from unity when $Z_{i,med}$ was used. For negative particle measurements, differences were found primarily when

d_p > 100 nm, but for positive particles, there was also a noticeable difference for particles smaller than 10 nm. This difference between the two polarities was likely caused by the negative ion mobility distribution being much more monodisperse than the positive one (Figure S1).

When the SR distribution was used, the observed biases in the inferred particle size distribution due to using $Z_{i,ave}$ or $Z_{i,med}$, instead of the whole ion mobility distribution were even smaller than when the measured distribution was used (Figure S9); The value of $R^*_{ave}(d_p)$ was within a factor of 1.05 from unity almost without exception, and, in general, the bias factor was smaller when $Z_{i,ave}$ was used than when $Z_{i,med}$ was used.

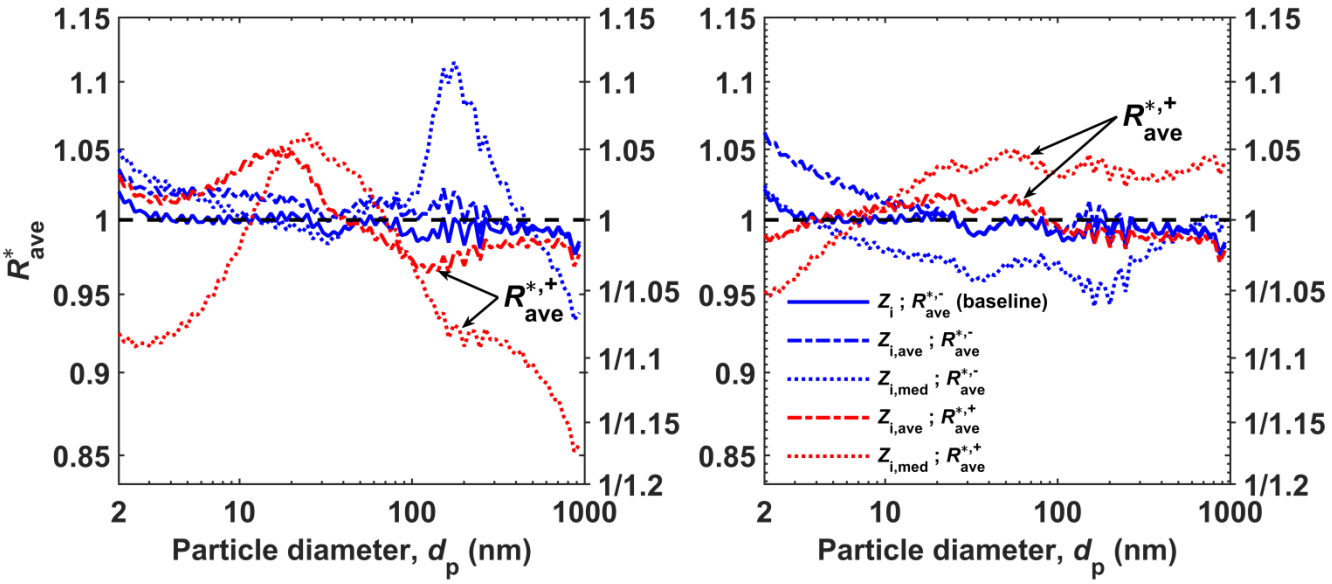

Figure S9. Left panel: The bias observed in the inferred particle size distribution when the measured ion mobility distribution, Z_i, was used when calculating $\boldsymbol{f}_{cha}$, but either the whole distribution, Z_i, mean mobility, $Z_{i,ave}$, or median mobility, $Z_{i,med}$, was used when calculating $\boldsymbol{f}_{inv}$, as indicated in the legend. The line color denotes the signal polarity. Right panel: As the left panel, except that the SR distribution was used.

A3.2 Bias in the inferred particle size distribution due to relative permittivity of charger ions

We examined the effect of the relative permittivity of the ion on the bias in the inferred particle size distribution. With the value of χ_i = 6 used when calculating $\boldsymbol{f}_{inv}$, a negligible bias in particle size distribution was observed regardless of the value used when calculating $\boldsymbol{f}_{cha}$, or whether the measured or SR distribution was used (Figure S10).

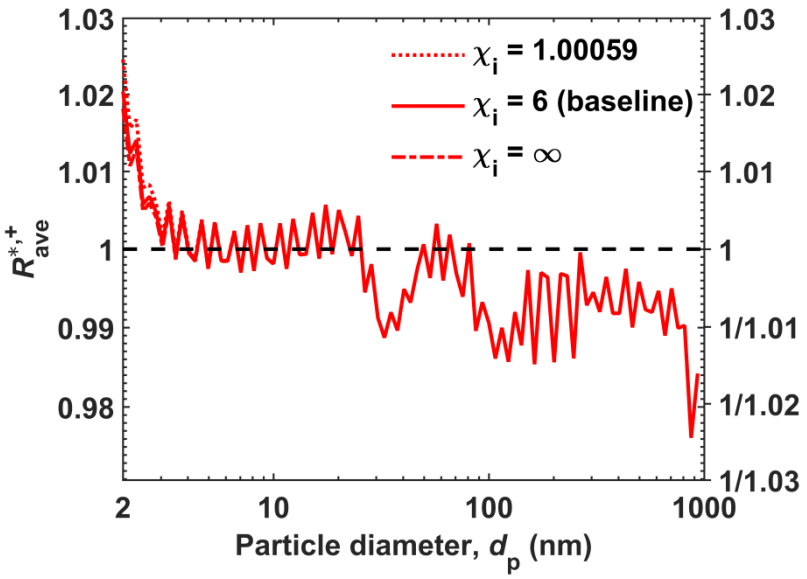

Figure S10. The bias observed in the inferred particle size distribution when the relative permittivity of ions, χ_i, was assumed to be ∞ (conductive), 6 (dielectric), or 1.00059 (air) when calculating $\boldsymbol{f}_{cha}$, but $\chi_i = 6$ was assumed when calculating $\boldsymbol{f}_{inv}$, as indicated in the legend. Only data for positive polarity when using the measured distribution is shown, as values for the negative polarity would not differ from the baseline case, and the biases observed when using the SR distribution were practically the same.

A3.3 Bias in the inferred particle size distribution due to limited value of q_{max} used in the inversion analysis

López-Yglesias and Flagan (2013a) showed that limiting the number of charge states considered may have a considerable effect on the calculated charge distribution: In this study, we set $k_{max} = 30$ when calculating any charge distribution. In order to lessen the computational burden, however, we only considered particles with ≤ 15 charges in the inversion analysis, i.e., $q_{max} = 15$; the effect of this truncation was negligible in comparison to calculations with $q_{max} = 30$. It should be noted that truncating the inversion charge distribution at $q_{max} = 15$ when the original charge distribution was calculated with $k_{max} = 30$ is a less constrained approximation than would occur if the original charge distribution had been calculated with $k_{max} = 15$: omitting charge states for which the fractional population would be considerable increases the fractional populations in the charge states that are taken into account (López-Yglesias and Flagan 2013a). The effect of reducing the q_{max} to 9 or 6 had little effect, but limiting it to 3 introduced a noticeable bias in the particle size distribution for $d_p > 100$ nm, regardless of whether the measured or SR distribution was used (Figure S11). It should be noted that the number of charges that should be taken into account in the inversion depends on the covered particle size range, as larger particles can acquire considerably more charges than do small ones.

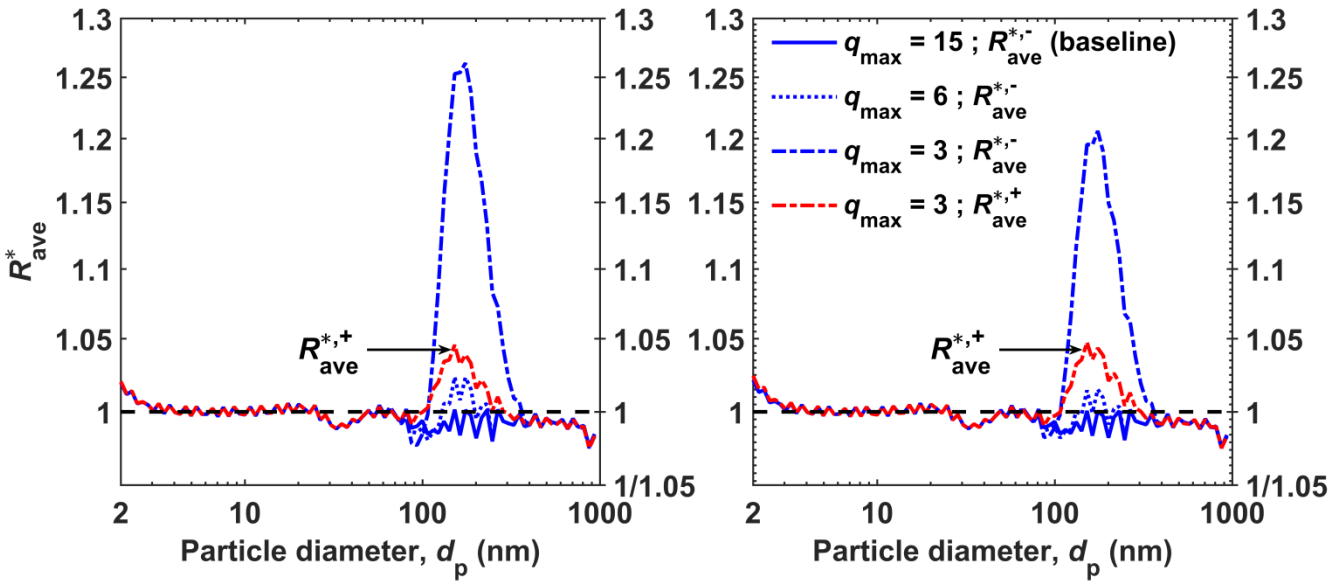

Figure S11. The bias observed in the inferred particle size distribution when up to 30 charges were considered when calculating the signal, but the number of charges considered in the inversion, q_{max}, was 15, 6 or 3. The line color denotes the signal polarity, with a noticeable difference between the polarities observed only when q_{max} = 3. The bias observed when using the measured and SR distributions are depicted on the left and right, respectively.

A4 The effect of the number of mobility channels and the shape of the triangular transfer function assumed in the pseudo-instrument on the bias in the inferred particle size distribution

As described in Sect. 2.3, the pseudo-instrument was assumed to have 100 mobility channels with the corresponding mobility equivalent diameters ranging from 1 to 1000 nm. Talukdar and Swihart (2003) operated a scanning mobility particle sizer with 300 channels covering diameters from 10 to 1000 nm to ensure that the resolution of their measurements was limited by the capabilities of the instrument and not by the number of channels. Neitola et al. (2011), on the other hand, operated a differential mobility particle sizer with 30 channels covering diameters from 10 to 800 nm. The number of channels per decade used in the present study falls short of that used by Talukdar and Swihart (2003), but is twice as high as the one used by Neitola et al. (2011). We chose the number of channels to be high enough to minimize the bias in the inferred particle size distribution due to sources other than the charge distribution. To assess how much this decision could affect the results reported in this study, we repeated some of the simulations using only 50 channels, which results in a number of channels per decade similar to those in typical differential mobility particle sizer measurements. Furthermore, we assumed that the transfer functions of the pseudo-instrument are triangles on a logarithmic mobility axis, while the ideal transfer functions, as presented by Knutson and Whitby (1975), are triangles on a linear mobility axis. To verify that our decision on the shape of the transfer function does not affect the results, we repeated some of the simulations using transfer functions that were triangles on a linear scale.

In the baseline case, the charge distribution acquired in the charger, $\boldsymbol{f}_{cha}$, and the one used in the inversion, $\boldsymbol{f}_{inv}$, were assumed to be the same, in which case there should be no charge distribution related bias in the inferred particle size distribution. As described in Sect. 3.1, when 100 channels were used in these conditions, the ratio of the inverted and simulated distributions, $R^*(d_p)$, fluctuated around unity due to numerical inaccuracies in the analysis, but very little systematic bias was observed in the inferred size distribution, with the value of $R^*_{ave}(d_p)$ being between 0.98 and 1.02 regardless of d_p. When 50 channels were used instead of 100, however, the fluctuation of R^* due to numerical inaccuracies was significantly smaller, but the bias observed in the inferred particle size distribution was slightly higher; depending on the simulation scenario and d_p, values of R^*_{ave} as low as 0.94 were observed, though in the range 3 nm < d_p < 400 nm, the value of R^*_{ave} was between 0.97 and 1.01 regardless of the simulation scenario (Figure S12). Whether the transfer function was a triangle on a logarithmic or linear mobility axis had negligible effect on the inferred size distribution.

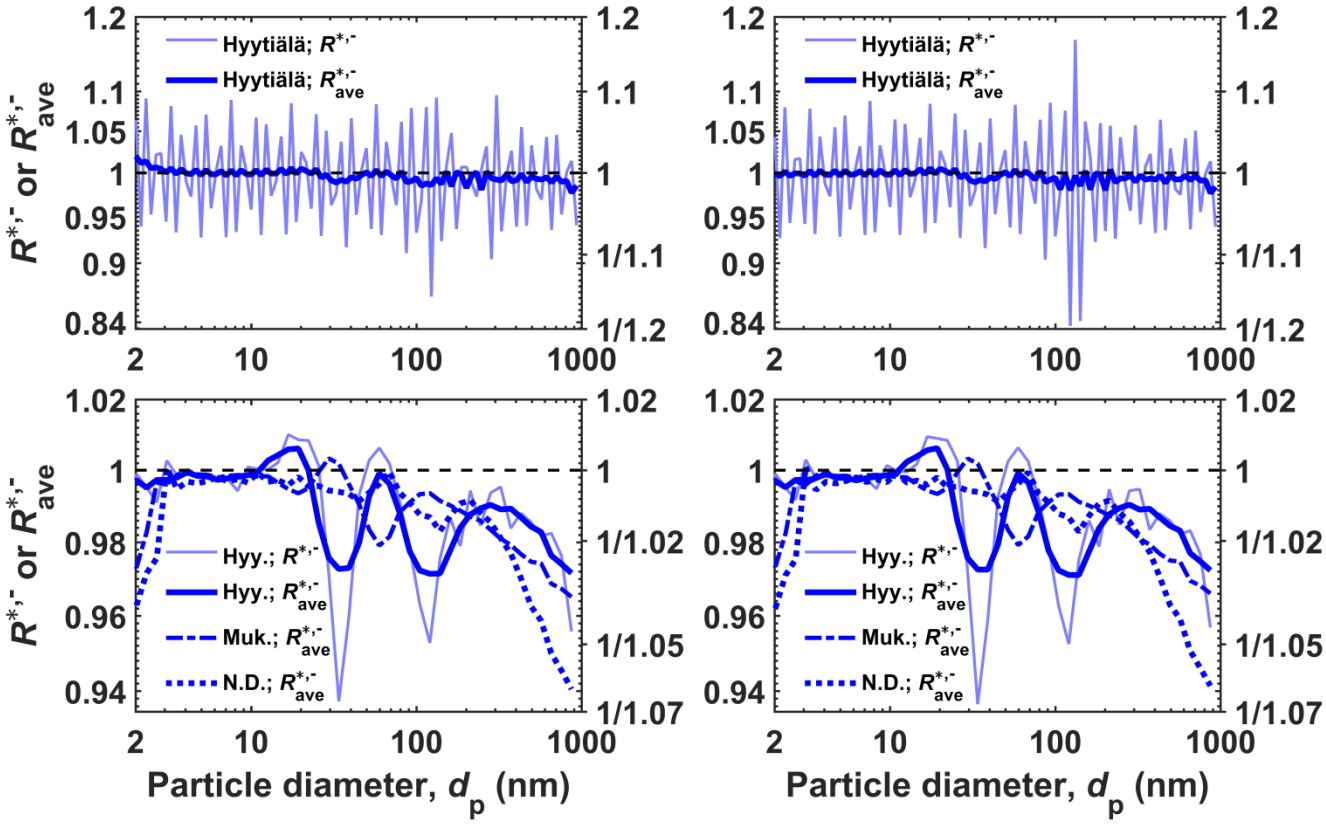

Figure S12. The bias observed in the inferred particle size distribution when the transfer function of a channel of the pseudo-instrument was assumed to be a triangle on a logarithmic mobility axis (left panels) or on a linear mobility axis (right panels), the number of channels of the pseudo-instrument was 100 (upper panels) or 50 (lower panels), $\boldsymbol{f}_{cha}$ and $\boldsymbol{f}_{inv}$ were the same, and the measured distribution was used. In the lower panels, the data are shown for Hyytiälä (Hyy.), Mukteshwar (Muk.) and New Delhi (N.D.) simulations. Note that the upper and lower panels have a different scale on the y-axis. Only the data when negative particles were counted is shown, but the results for positive polarity were very similar.

To verify that the results given above were not unique to the baseline case, i.e., when $\boldsymbol{f}_{cha} = \boldsymbol{f}_{inv}$, we repeated the analysis for several conditions in which $\boldsymbol{f}_{cha} \neq \boldsymbol{f}_{inv}$. An example of such a test is depicted in Figure S13, and the conclusion is the same as before: the number of channels has only little effect and the shape of the transfer function has negligible effect on the bias in the inferred size distribution.

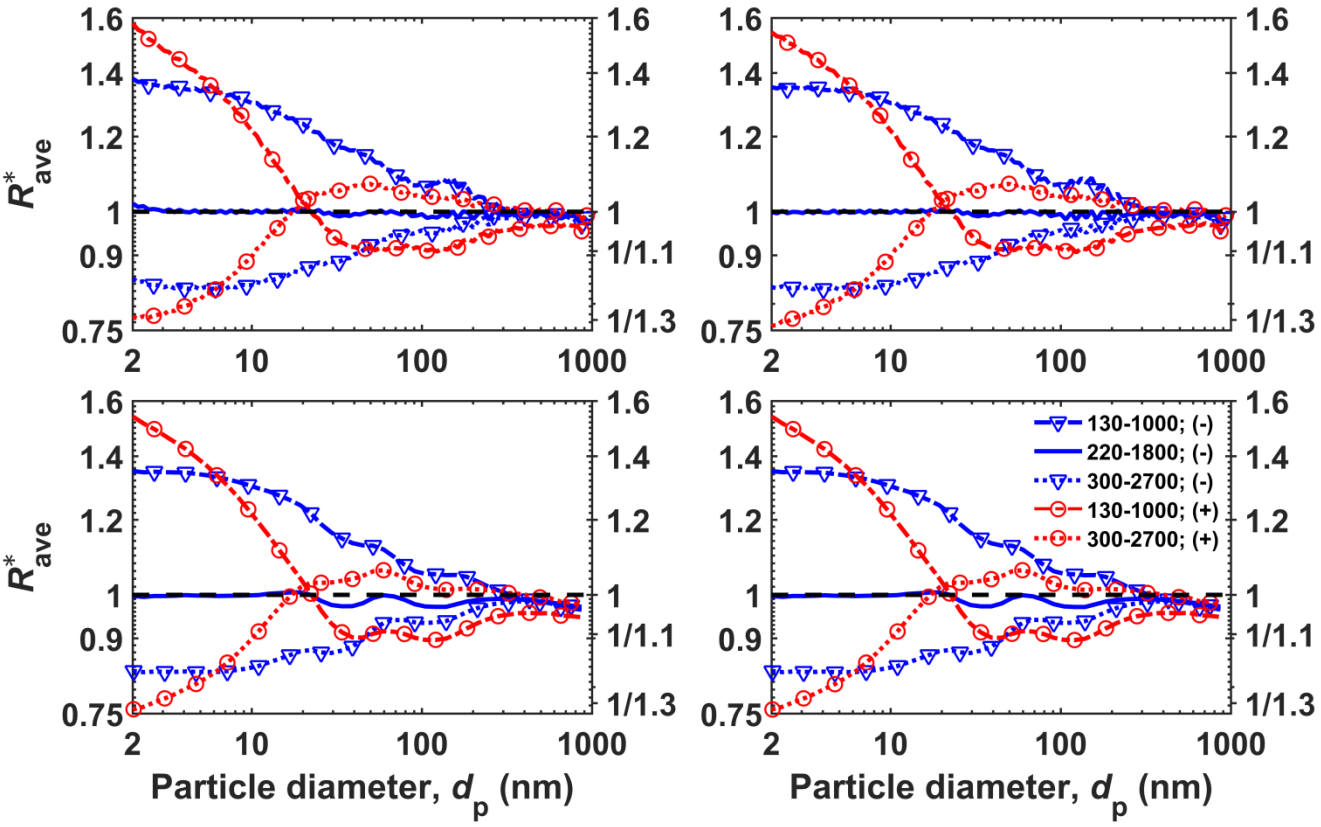

Figure S13. The bias observed in the inferred particle size distribution when the ion masses ranged from 130 to 1000 Da (ρ_i = 800 kg m^{-3}), from 220 to 1800 Da (ρ_i = 1500 kg m^{-3}), or from 300 to 2700 Da (ρ_i = 2200 kg m^{-3}) when calculating $\boldsymbol{f}_{cha}$, but were from 220 to 1800 Da when calculating $\boldsymbol{f}_{inv}$, as indicated in the legend. The transfer function of a channel of the pseudo-instrument was assumed to be a triangle on a logarithmic mobility axis (left panels) or on a linear mobility axis (right panels), the number of channels of the pseudo-instrument was 100 (upper panels) or 50 (lower panels), and the measured distribution was used. Whether negative or positive particles were counted is indicated by (-) and (+), respectively, in the legend.

References:

Flagan, R. C. (2004). Opposed migration aerosol classifier (OMAC). *Aerosol Sci. Technol.*, *38*(9): 890–899.

Gopalakrishnan, R., Meredith, M. J., Larriba-Andaluz, C., and Hogan, C. J. (2013). Brownian dynamics determination of the bipolar steady state charge distribution on spheres and non-spheres in the transition regime. *J. Aerosol Sci.*, 63:126–145.

Gopalakrishnan, R., McMurry, P. H., and Hogan, C. J. (2015). Bipolar Charging of Nanoparticles: A Review and Development of Approaches for Non-spherical Particles. *Aerosol Sci. Technol.*, 49:1181–1194.

Hoppel, W. A., and Frick, G. M. (1986). Ion-Aerosol Attachment Coefficients and the Steady-State Charge Distribution on Aerosols in a Bipolar Ion Environment. *Aerosol Sci. Technol.*, 5:1–21.

Hussin, A., Scheibel, H. G., Becker, K. H., and Porstendörfer, J. (1983). Bipolar diffusion charging of aerosol particles—1: experimental results within the diameter range 4–30 nm. *J. Aerosol Sci.*, 14(5):671–677.

Knutson, E. O., and Whitby, K. T. (1975). Aerosol Classification by Electric Mobility: Apparatus, Theory and Applications. *J. Aerosol Sci.*, 6:443–451.

Lee, H. M., Kim, C. S., Shimada, M., and Okuyama, K. (2005). Effects of Mobility Changes and Distribution of Bipolar Ions on Aerosol Nanoparticle Diffusion Charging. *J. Chem. Eng. Jpn.*, 38:486–496.

López-Yglesias, X., and Flagan, R. (2013a). Population balances of micron-sized aerosol in a bipolar ion environment. *Aerosol Sci. Technol.*, 47(6):681–687.

López-Yglesias, X., and Flagan, R. (2013b). Ion-aerosol flux coefficients and the steady state charge distribution of aerosols in a bipolar ion environment. *Aerosol Sci. Technol.*, 47(6):688–704.

Mai, H. (2016). Personal communication.

Maißer, A., Thomas, J. M., Larriba-Andaluz, C., He, S., and Hogan, C. J. (2015). The mass-mobility distributions of ions produced by a Po-210 source in air. *J. Aerosol Sci.*, 90:36–50.

Mui, W., Thomas, D. A., Downard, A. J., Beauchamp, J. L., Seinfeld, J. H., and Flagan, R. C. (2013). Ion Mobility-Mass Spectrometry with a Radial Opposed Migration Ion and Aerosol Classifier (ROMIAC). *Anal. Chem.*, 85(13):6319–6326, doi:10.1021/ac400580u.

Mui, W., Mai, H., Downard, A. J., Seinfeld, J. H., and Flagan, R. C. (2017). Design, simulation, and characterization of a radial opposed migration ion and aerosol classifier (ROMIAC). *Aerosol Sci. Tech.*, advance online publication, doi: 10.1080/02786826.2017.1315046.

Neitola, K., Asmi, E., Komppula, M., Hyvärinen, A.-P., Raatikainen, T., Panwar, T. S., Sharma, V. P., and Lihavainen, H. (2011). New particle formation infrequently observed in Himalayan foothills – why? *Atmos. Chem. Phys.*, 11:8447–8458, doi:10.5194/acp-11-8447-2011.

Steiner, G., and Reischl, G. P. (2012). The effect of carrier gas contaminants on the charging probability of aerosols under bipolar charging conditions. *J. Aerosol Sci.*, 54:21–31.

Steiner, G., Jokinen, T., Junninen, H., Sipilä, M., Petäjä, T., Worsnop, D. R., Reischl, G. P., and Kulmala, M. (2014). High-Resolution Mobility and Mass Spectrometry of Negative Ions Produced in a 241Am Aerosol Charger. *Aerosol Sci. Technol.*, 48(3):261–270, doi:10.1080/02786826.2013.870327.

Stolzenburg, M. R. (1988). An Ultrafine Aerosol Size Distribution Measuring System, University of Minnesota, Minneapolis.

Talukdar, S. S., and Swihart, M. T. (2003). An Improved Data Inversion Program for Obtaining Aerosol Size Distributions from Scanning Differential Mobility Analyzer Data. *Aerosol Sci. Technol.*, 37(2):145–161, doi: 10.1080/02786820390112632.

Wiedensohler, A. (1988). An Approximation of the Bipolar Charge Distribution for Particles in the Submicron Size Range. *J. Aerosol Sci.*, 19:387–389.